# Synthesis of "Naked" TeO$_2$ Nanoparticles for Biomedical Applications

Tina Hesabizadeh, Evan Hicks, David Medina Cruz, Shawn E. Bourdo, Fumiya Watanabe, Marvin Bonney, John Nichols, Thomas J. Webster, and Grégory Guisbiers*

Read Online

ACCESS | 📊 Metrics & More | 📑 Article Recommendations

**ABSTRACT:** Chalcogenide nanoparticles have become a very active field of research for their optoelectronic and biological properties. This article shows the production of tellurium dioxide nanoparticles (TeO$_2$ NPs) by pulsed laser ablation in liquids. The produced nanoparticles were spherical with a diameter of around 70 nm. The energy band gap of those nanoparticles was determined to be around 5.2 eV. Moreover, TeO$_2$ NPs displayed a dose-dependent antibacterial effect against antibiotic-resistant bacteria such as multidrug-resistant *Escherichia coli* (MDR *E. coli*) and methicillin-resistant *Staphylococcus aureus* (MR *S. aureus*). The "naked" nature of the nanoparticle surface helped to eradicate the antibiotic-resistant bacteria at a very low concentration, with IC50 values of ∼4.3 ± 0.9 and 3.7 ± 0.2 ppm for MDR *E. coli* and MR *S. aureus*, respectively, after just 8 h of culture. Further, the IC50 values of the naked TeO$_2$ NPs against melanoma (skin cancer) and healthy fibroblasts were 1.6 ± 0.7 and 5.5 ± 0.2 ppm, respectively, for up to 72 h. Finally, to understand these optimal antibacterial and anticancer properties of the TeO$_2$ NPs, the reactive oxygen species generated by the nanoparticles were measured. In summary, the present in vitro results demonstrate much promise for the presently prepared TeO$_2$ NPs and they should be studied for a wide range of safe antibacterial and anticancer applications.
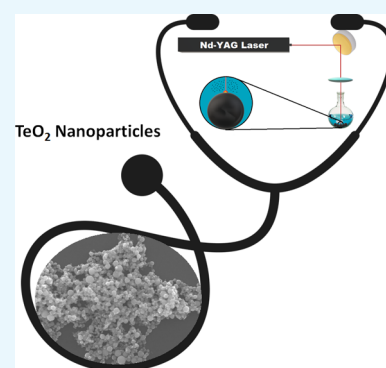
## 1. INTRODUCTION

Tellurium(Te) is one of the rarest chemical elements in the Earth's crust.[1−4] Its large absence on Earth finds its origin in Earth's formation when Te is bound to hydrogen to form tellurium hydrides. Earth's gravity was not strong enough to retain these highly volatile hydrides, and most Te escaped into space, making it rare on Earth but not in the Universe.[5] Nevertheless, Te forms compounds that are of great interest to the scientific community, mainly due to their optoelectronic properties and a wide array of biological properties whose research has been gaining interest over the last few decades. For example, cadmium telluride (CdTe) is used in flexible solar cells, displaying a 16.4% efficiency,[6] while copper telluride (Cu$_2$Te) is a thermoelectric material exhibiting a figure of merit (ZT) of around 1.1.[7,8] In terms of their biological properties, most alkali−metal tellurites and tellurates are useful in microbiology, while the antioxidant effects of organotellurides and diorganoditellurides and the immunomodulatory effects of the nontoxic inorganic tellurane, named AS-101, are also of great interest in research.[9,10]

One of the most simple Te-based compounds is its oxide, tellurium dioxide (TeO$_2$), which is an important catalyst in oxidation, hydrogenation, and dehydrogenation processes.[11] TeO$_2$ is a polymorph material that exhibits three crystalline structures: $\alpha$-TeO$_2$ (paratellurite, gray color), $\beta$-TeO$_2$ (tellurite, yellow color), and $\gamma$-TeO$_2$ (metastable).[12−14] $\alpha$-

TeO$_2$ displays an indirect band gap of around 2.9 eV and a direct band gap of around 3.3 eV.[15] $\beta$-TeO$_2$ displays only a direct band gap of around 2.2 eV, while $\gamma$-TeO$_2$ only exhibits an indirect band gap of around 3.1 eV.[15] That is why TeO$_2$ is also used in fiber optics and waveguide applications.[16] Indeed, the visible portion of the electromagnetic spectrum ranges from 1.6 to 3.3 eV; therefore, with TeO$_2$ nanostructures displaying energy band gaps larger than ∼3.3 eV, visible light will be easily transmitted through those structures.

One of the earliest applications of TeO$_2$ in biomedical applications came from its use as an antibiotic.[10] Indeed, in the pre-penicillin era, Te-based compounds were used by Alexander Fleming to inhibit the growth of many pathogens.[17] Tellurium itself is not particularly toxic but its absence in the biological world may explain its efficacy against pathogens.[10] When used in the nanometer size range, Te-based compounds, including TeO$_2$, provide a dramatic improvement in their biomedical properties due to an increase in their surface-to-volume ratios and a sustained increase in reactivity with
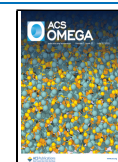
**Table 1. List of Studies Discussing the Synthesis of Te and TeO$_2$ NPs by PLAL[a,b]**

| authors | Khalef[37] | Liu et al.[28,38] | Guisbiers et al.[29] | Saraeva et al.[39] | Khalef et al.[40] | this work |
|---|---|---|---|---|---|---|
| publication year | 2014 | 2016 | 2017 | 2020 | 2021 | 2022 |
| type of laser | Nd:YAG | Nd:YAG | Nd:YAG | Yb-doped | Nd:YAG | Nd:YAG |
| wavelength (nm) | 1064 | 1064 | 1064 | 1040 | 1064 | 1064 |
| repetition rate (Hz) | 1 | 20 | 20 | 20,000 | 1 | 1,000 |
| pulse duration (ns) | ~9 | ~10 | ~4 | ~120 | ~9 | ~100 |
| irradiation time (s) | 20 | 2, 10, 180 | 900 | | 50 | 300 |
| solvent | deionized (DI) water | DI water, methanol, ethanol, acetone, dichloromethane | DI water, acetone | DI water | DI water | DI water |
| target | static | static | static | dynamic | static | static |
| fluence (J/cm$^2$) | | ~11 | ~2 | | | ~284 |
| product | TeO$_2$ NPs | TeO$_2$ NPs, Te NPs, | TeO$_2$ NPs, Te NPs | TeO$_2$ NPs | TeO$_2$ NPs | TeO$_2$ NPs |
| application | none | none | none | antibacterial: *S. aureus* biofilms | antibacterial: *E. coli*, *S. aureus* | • antibacterial: MDR *E. coli*, MR *S. aureus* <br> • anticancer: human melanoma cells |

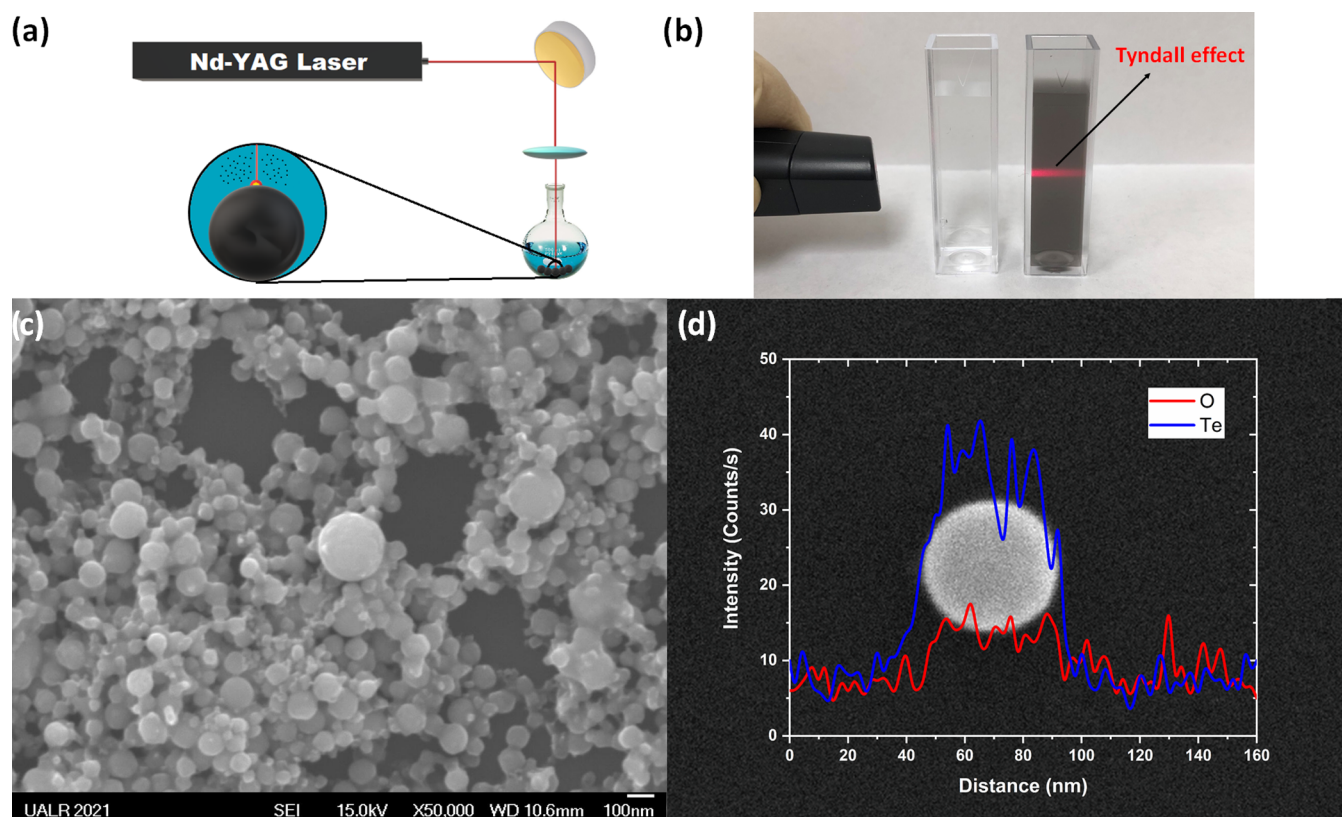[a]Nd:YAG, neodymium-doped:yttrium aluminum garnet. [b]NPs, nanoparticles.



**Figure 1.** (a) Sketch showing the PLAL synthesis protocol. (b) Tyndall effect observed on the colloid synthesized by PLAL at 1000 Hz. The left solution is the solvent, i.e., DI water, while the right solution is the colloid containing the TeO$_2$ NPs. (c) Scanning electron microscopy (SEM) image of the TeO$_2$ NPs contained in the colloid synthesized by PLAL at 1000 Hz. (d) Energy-dispersive X-ray (EDX) line scan through one TeO$_2$ particle.

biological membranes. Therefore, Te-based nanoparticles (NPs) can be employed in antibacterial applications, as the sole agent,[18] or in combination with bioactive glasses[19] or anticancer approaches.[20−23]

One of the most important factors impacting the applicability and activity of any NP is how they are made and the presence of synthetic byproducts in their final form. Nowadays, TeO$_2$ NPs are synthesized by various techniques
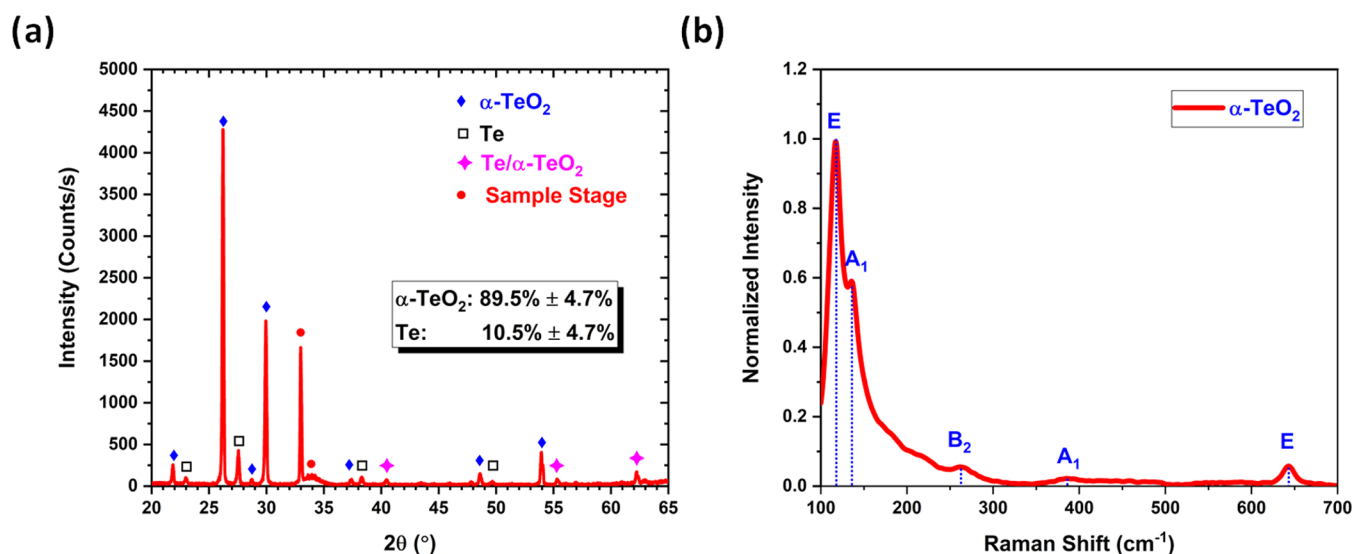
**Figure 2.** (a) XRD spectra. The peak positions of Te and $\alpha$-TeO$_2$ were obtained from the crystallography open database entries 1011098 and 1530871, respectively. (b) Raman spectra.

such as biosynthesis,[24] spray pyrolysis,[25] thermal evaporation,[26] sonochemistry,[27] and pulsed laser ablation in liquids (PLAL).[28,29] Among these techniques, PLAL is the one that creates NPs with a clean surface (i.e., without any surfactants or impurities attached), allowing them to interact efficiently with their environment. This advantage is particularly suitable for catalytic[30−32] and antibacterial[33−35] applications.

Therefore, this paper focused on the synthesis of "naked" TeO$_2$ NPs by PLAL. The originality of our PLAL synthesis lies in the use of a high repetition rate (1 kHz) pulsed laser when irradiating a static Te target. As featured in Table 1, this study is the first to report the ablation of a pure static Te target in the kHz regime. By increasing the repetition rate from 100 Hz to 1 kHz, we noticed an increase of 36% in the production rate of TeO$_2$ NPs. Consequently, the synthesis time can be significantly abridged to produce the same amount of NPs, as already noticed by Nikolov et al. in the case of silver NPs.[36] Furthermore, this is the first time that TeO$_2$ NPs produced by PLAL are tested against antibiotic-resistant bacteria such as multidrug-resistant *Escherichia coli* (MDR *E. coli*), methicillin-resistant *Staphylococcus aureus* (MR *S. aureus*), and a cancer cell specifically human melanoma cells.

## 2. MATERIALS AND METHODS

**2.1. PLAL Synthesis.** TeO$_2$ NPs were synthesized by utilizing a nanosecond Nd:YAG laser (Electro Scientific Industries) operating at 1064 nm. The pulsed laser beam was reflected off a gold-coated mirror oriented at a 45° angle with respect to the laser rail (Figure 1a). A biconvex lens (focal length = 83 mm) was placed on the laser beam path between the mirror and the target to focus the beam on the target's surface. The laser beam's spot size on the target's surface was measured at around ∼45 $\mu$m. Consequently, the fluence of the laser was determined to be around ∼346 J cm$^{-2}$. Indeed, the laser's pulse repetition rate was fixed at 1 kHz with an energy output per pulse of around 5.5 mJ. However, as liquid water absorbs the 1064 nm radiation, it is important to consider the effect of the liquid height on the fluence. Here, the liquid height on top of the target was set at 8 mm. Therefore, according to Hamad et al.,[41] the fluence was reduced by ∼18%,

giving a value of around ∼284 J cm$^{-2}$. The target consisted of bulk Te pellets (99.99% from Sigma-Aldrich 263303-25G), ∼2 mm in diameter, and the pellets were sitting immobile at the bottom of a 50 mL rounded single-neck glass flask. The flask was then filled with 5 mL of deionized (DI) water. The NPs were produced by irradiating the static target for 5 min.

**2.2. Physicochemical Characterization.** After synthesis, the samples were characterized by ultraviolet (UV)−visible spectroscopy (Cary 5000 from Agilent), Raman spectroscopy (EZRaman-I Series from TSI), atomic emission spectroscopy (AES, 4210 MP-AES from Agilent), dynamic light scattering (DLS, NanoBrook 90Plus DLS from Brookhaven Instruments Corporation), scanning electron microscopy (SEM, JEOL JSM 7000F SEM, operating at 15 kV), differential scanning calorimetry (DSC, Mettler Toledo), X-ray photoelectron spectroscopy (XPS, Thermo Fisher K$\alpha$), and X-ray diffraction (XRD, Rigaku Miniflex 600). The Raman, DSC, XPS, and XRD spectra were collected from dried sedimentation present after centrifugation of the colloid. For SEM analysis, a droplet of the colloid was deposited onto a silicon wafer, which was then dried in an environmentally controlled glovebox.

**2.3. Biological Characterization.** Strains of one Gram-negative, multidrug-resistant *E. coli* (MDR *E. coli*) (ATCC BAA-2471; ATCC, Manassas, VA) bacteria, and one Gram-positive, methicillin-resistant *S. aureus* (MR *S. aureus*) (ATCC 4330; ATCC, Manassas, VA) bacteria, were used in this study to determine the antibacterial activity of the TeO$_2$ NPs after 8 h of culture. Both bacteria were cultured according to the ATCC instructions. The entire protocol is described in refs 42, 43. All experiments were repeated in triplicate ($N = 3$) unless otherwise indicated to ensure the reliability of the results. Statistical significance was assessed using Student's $t$-tests, setting an $\alpha$ value of less than 0.05 as statistically significant compared to the controls. Results were displayed as the mean ± standard deviation using Prism 9 software, 2021 version. Relevant parameters to the biomedical use of the NPs were calculated following modeling methods in the same software.

Reactive oxygen species (ROS) were quantified using 2′,7′-dichlorodihydrofluorescein diacetate (H2DCFDA) following the instructions of the kit. Briefly, human melanoma cells were seeded in a 96-well plate in the presence of different
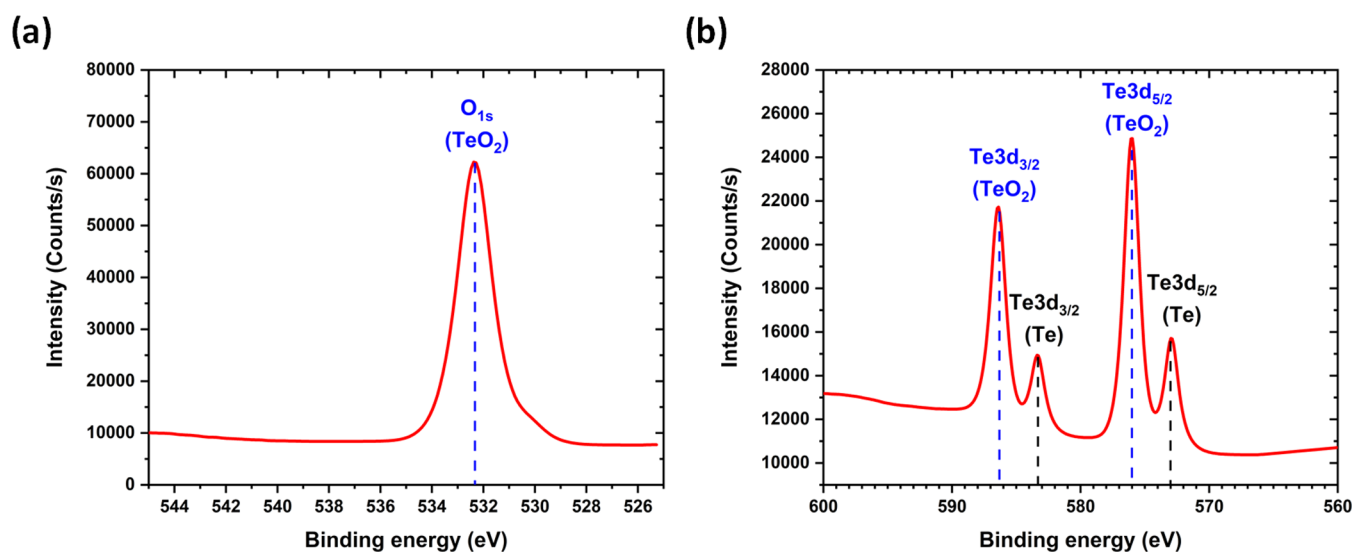
**Figure 3.** (a) XPS spectra focusing on the O 1s orbitals. (b) XPS spectra focusing on the Te 3d orbitals. For Te 3d spectrum fitting, the best fit Lorentzian−Gaussian ratio was 28.05% for $TeO_2$ and 71.44% for the metallic Te.
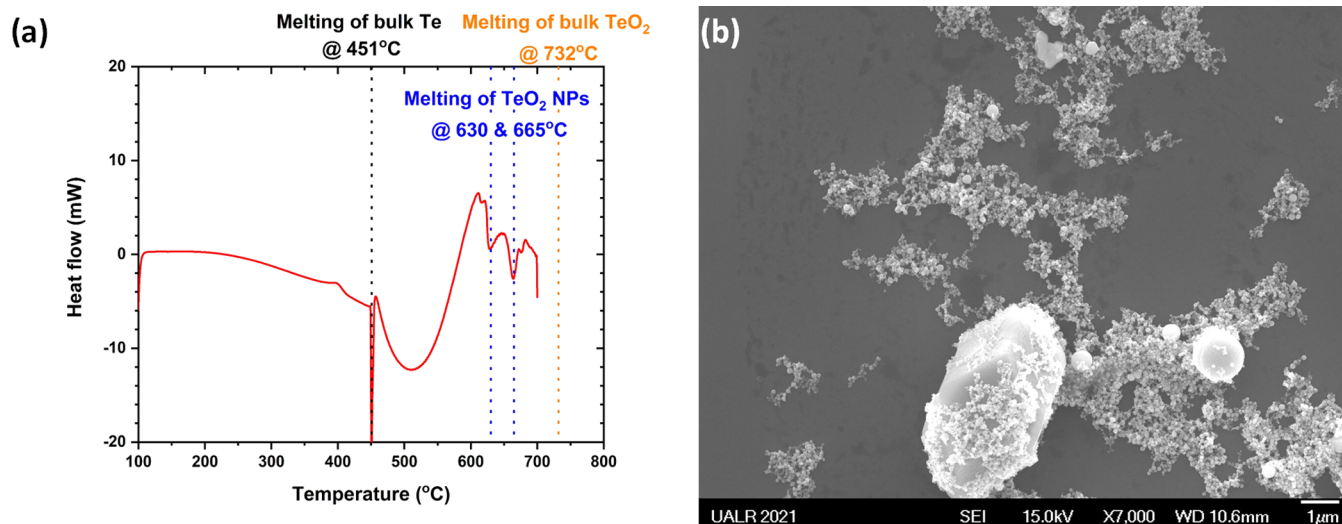


**Figure 4.** (a) Differential scanning calorimetry curve. (b) SEM image showing $TeO_2$ NPs and Te ablation debris from the target.

concentrations of nanoparticles with the appropriate positive and negative controls. The ROS indicator was reconstituted in anhydrous dimethyl sulfoxide (DMSO), the cell medium was then removed, and the cells were washed twice with buffer. Afterward, a fixed volume of the indicator in phosphate-buffered saline (PBS) was added to each one of the wells at a final concentration of 10 $\mu$M. The cells were incubated for 30 min, and fresh medium was added, and the cells were allowed to recover for a short time. Positive controls were included, stimulating the oxidative activity with hydrogen peroxide to a final concentration of 50 $\mu$M. The intensity of fluorescence was then observed by flow cytometry at 530 nm when the sample was excited at 485 nm.

## 3. RESULTS AND DISCUSSION

**3.1. Physicochemical Tests.** To be classified as a colloid, the liquid-containing structures should scatter the laser light and make the laser beam visible when shining a laser pointer through the colloid. This effect is known as the Tyndall effect.[44,45] In Figure 1b, two cuvettes are displayed: the left one

is filled with DI water and serves as a reference, while the right one is our sample. By looking at the reference cuvette, the laser beam is not visible as the size of the water molecules was too small compared to the pointer laser wavelength (~650 nm). However, the laser beam becomes visible when going through the sample, consequently, confirming the presence of NPs within the liquid (Figure 1b). The gray color of our colloidal solution is similar to that observed by Khalef et al.[37] who also synthesized $TeO_2$ NPs by PLAL. The NPs were then observed by SEM, as shown in Figure 1c, where the shape of NPs was identified as being spherical. The EDX line scan across one spherical NP confirmed that $TeO_2$ was formed uniformly across the NP (Figure 1d).

Further investigation by XRD (Figure 2a) confirmed that the colloid was made of $\alpha$-$TeO_2$ (89.5 ± 4.7%) and Te (10.5 ± 4.7%). The crystalline phase of $\alpha$-$TeO_2$ was then further identified by Raman spectroscopy by displaying peaks at 116 $cm^{-1}$ (E), 136 $cm^{-1}$ ($A_1$), 262 $cm^{-1}$ ($B_2$), 386 $cm^{-1}$ ($A_1$), and 644 $cm^{-1}$ (E)[13,46] (Figure 2b). Clearly, the phonon states in $TeO_2$ can be distinguished into two groups: librational and
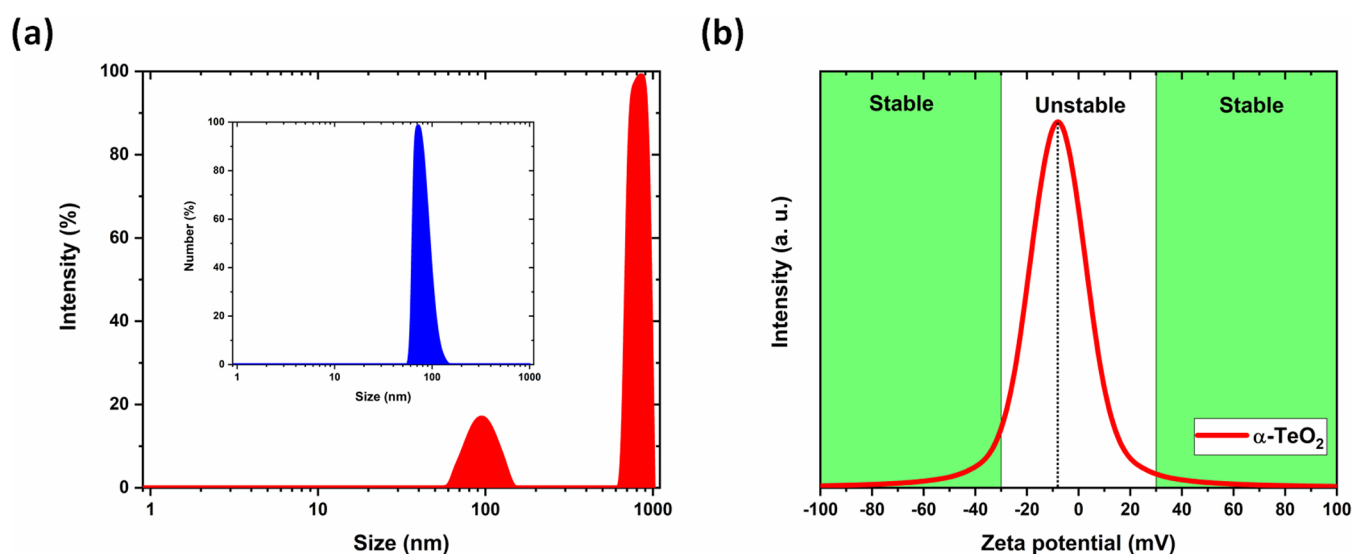
**Figure 5.** (a) Intensity size distribution as measured by DLS on the colloid synthesized at 1000 Hz. Inset: number size distribution measured by DLS on the colloid synthesized at 1000 Hz. The number size distribution is centered around ∼70 nm. (b) The $\zeta$-potential was measured to be $-8 \pm 1$ mV, meaning that the colloid was not stable with time.
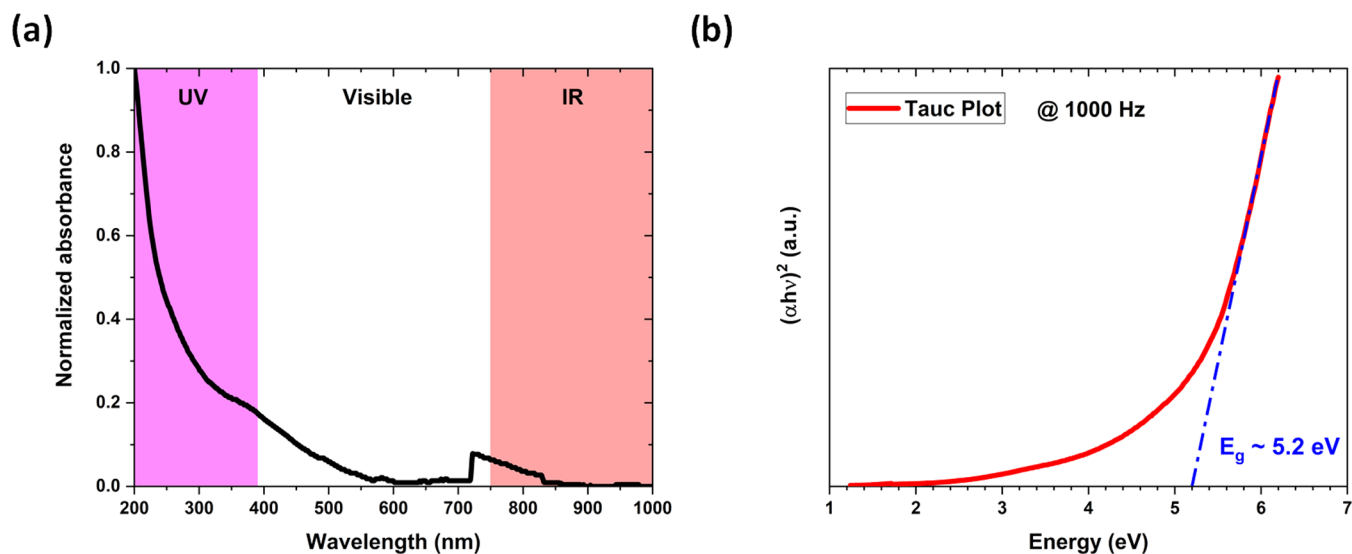


**Figure 6.** (a) UV−visible spectra of the colloid shown in Figure 1b. (b) Tauc plot displaying an energy band gap of around ∼5.2 eV.

deformational.[47] The two modes at frequencies lower than 150 cm$^{-1}$ correspond to the librational modes of TeO$_4$ units.[48] Indeed, the Te atoms in the $\alpha$-TeO$_2$ paratellurite structure have four neighboring O atoms so that the elementary structural unit is a TeO$_4$ disphenoid, and from such TeO$_4$ units sharing corners, the $\alpha$-TeO$_2$ paratellurite structure is built. The three modes at frequencies above 150 cm$^{-1}$ correspond to the deformational modes of the TeO$_4$ units. Specifically, the B$_2$ mode at 262 cm$^{-1}$ is a stretching mode of the Te−O chemical bond; the A$_1$ mode at 386 cm$^{-1}$ corresponds to the bending mode of O−Te−O, and the E mode at 644 cm$^{-1}$ corresponds to the stretching mode of the Te−O chemical bond.

XPS was performed to determine the surface state of the TeO$_2$ NPs (Figure 3). The software Avantage from Thermo Scientific was used for the acquisition and analysis. Avantage uses a mixture of Gaussian and Lorentzian to fit the peaks; the mixture ratio can be fixed or be a variable in the fitting routine. The O 1s peak found around ∼530 eV is assigned to the

existence of bridging oxygen atoms Te−O−Te[49] (Figure 3a). Furthermore, it is possible to identify the Te oxidation states using the satellite peak features of Te 3d (Figure 3b). There are strong satellite peaks around ∼576 and ∼586 eV indicating the presence of TeO$_2$ at the surface, while there are two weak peaks around ∼573 and ∼583 eV indicating the presence of Te.[50] Based on the surface area of the peaks corresponding to TeO$_2$ and Te, the TeO$_2$/Te ratio is around ∼3, meaning that there is 3 times more TeO$_2$ in the colloid than in Te, i.e., ∼75% of the colloid is made of TeO$_2$, while ∼25% is made of Te (Figure 3b). Remember that XPS is a surface analysis technique, which is why there is a slight discrepancy concerning the TeO$_2$/Te ratio with the XRD measurements as XRD also measures the core of the NPs and not only the surface. It means that TeO$_2$ is not only found at the surface of the NPs but also located at the very core.

The colloid was then analyzed by differential scanning calorimetry (DSC). The reason for performing DSC (Figure 4a) is to demonstrate that there are no Te nanoparticles within
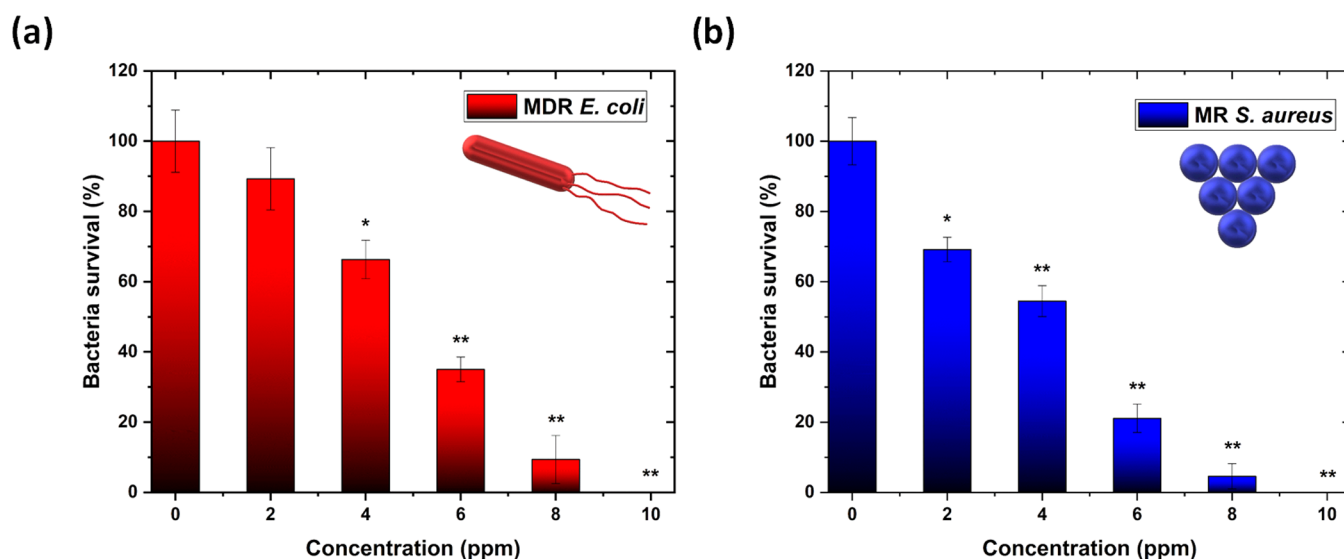
**Figure 7.** Colony counting assay of (a) MDR *E. coli* and (b) MR *S. aureus* for 8 h in the presence of different concentrations of TeO$_2$ NPs. All values represent the mean $\pm$ standard deviation. *$p < 0.05$, **$p < 0.01$ (compared to controls).

the colloid and clearly identify that the origin of Te detected by XRD comes from some chunks or dust of the Te target that got detached during the irradiation. Indeed, the first peak popping up at 451 °C in Figure 4a corresponds to the bulk melting temperature of Te, but no peaks appear below 451 °C, consequently confirming the absence of Te nanoparticles. There are also two other peaks appearing at 630 and 665 °C, which corresponds to two populations of TeO$_2$ NPs. Indeed, those peaks appeared above 451 °C and below 732 °C, which is the bulk melting temperature of TeO$_2$; therefore, those two populations cannot be made out of Te but should be made of TeO$_2$ displaying nanometer size dimensions, as the melting temperature of the nanoparticles decreased with the size of the nanoparticle.[51,52] Figure 4b shows the TeO$_2$ NPs and some Te ablation debris coming from the target.

Further investigation was performed by dynamic light scattering (DLS) to determine the size distribution of the NPs. Based on Figure 5a, there seem to be two main populations of NPs within the colloid, one around ∼70 nm and another around ∼800 nm. By converting the intensity size distribution into a number size distribution, there was only one population around ∼70 nm, suggesting that the second population (∼800 nm in size) observed in the intensity size distribution comes from the agglomeration of the NPs belonging to the first population (∼70 nm in size) or from microscopic chunks/dust of the target being ejected upon the impact of the laser beam. To confirm the possible agglomeration of NPs, the ζ-potential of the NPs was determined and found to be around −8 ± 1 mV, which is well below the threshold value of 30 mV corresponding to a stable colloid (Figure 5b). Consequently, the value of ζ-potential confirmed the instability of TeO$_2$ NPs with time. To be complete, the pH of the colloid was measured at 5.2 ± 0.1.

By using UV−visible spectroscopy (Figure 6a), the direct energy band gap of the TeO$_2$ NPs was measured at around ∼5.2 eV (Figure 6b). This value is in excellent agreement with the value reported by Khalef et al.[40] who measured a value of ∼5 eV for TeO$_2$ NPs having sizes around ∼55 nm. The strong absorption band in the UV region of the absorbance spectra (Figure 6a) is due to the transition from the valence band (p-

nonbonding triplet) to the conduction band (p-antibonding triplet) of TeO$_2$.

**3.2. Biological Tests.** Finally, within those synthesis conditions, TeO$_2$ spherical NPs with a "naked" surface and a size distribution of around ∼70 nm were obtained, which is in the optimal size range to interact with biological cells.[53,54] Consequently, the spherical TeO$_2$ NPs were tested against MDR *E. coli* and MR *S. aureus*, two harmful pathogens, one Gram-negative and one Gram-positive, that developed a resistance to antibiotics (Figure 7). The NPs were active against both pathogens at a range of concentrations between 2 and 10 ppm, showing a clear dose-dependent inhibition that was more lineal and substantial in MR *S. aureus*. Indeed, the cell wall of Gram-positive bacteria such as MR *S. aureus* includes a layer of peptidoglycan as well as teichoic acid and abundant pores that allow foreign nanoparticles to penetrate, resulting in cell membrane damage and cell death, while the cell wall of Gram-negative bacteria such as MDR *E. coli* is composed of lipopolysaccharides, lipoproteins, and phospholipids, which form a penetration barrier to nanoparticles.[55] Therefore, the TeO$_2$ NPs showed an effective bacterial inhibition at concentrations of ∼10 ppm, which was much less than the concentration of ∼25 ppm of selenium (Se) NPs prepared also by PLAL required to fully inhibit the growth of MR *S. aureus* and MDR *E. coli* in a previous study.[33] The size distribution of those Se NPs was centered around 43 ± 20 nm. Consequently, the TeO$_2$ NPs were more effective than the Se NPs synthesized by the same technique in terms of antimicrobial effectiveness. As TeO$_2$ (oxidation state +4) and Se (oxidation state 0) are both chalcogenide compounds, bacteria are using the same metabolic machinery associated with sulfur (S) in the production of amino acids; therefore, the difference in their antibacterial efficiency could come from their oxidation state being different. Another possible cause of TeO$_2$'s higher efficiency is its ability to interact with Se present in some selenoproteins and enzymes, which could disturb the vital functions of the bacteria.[3,10]

The minimum inhibitory concentration (MIC) values were calculated to quantify the static effects of the NPs in the studied bacterial strains. MIC values were 4.3 ± 0.9 and 3.7 ±
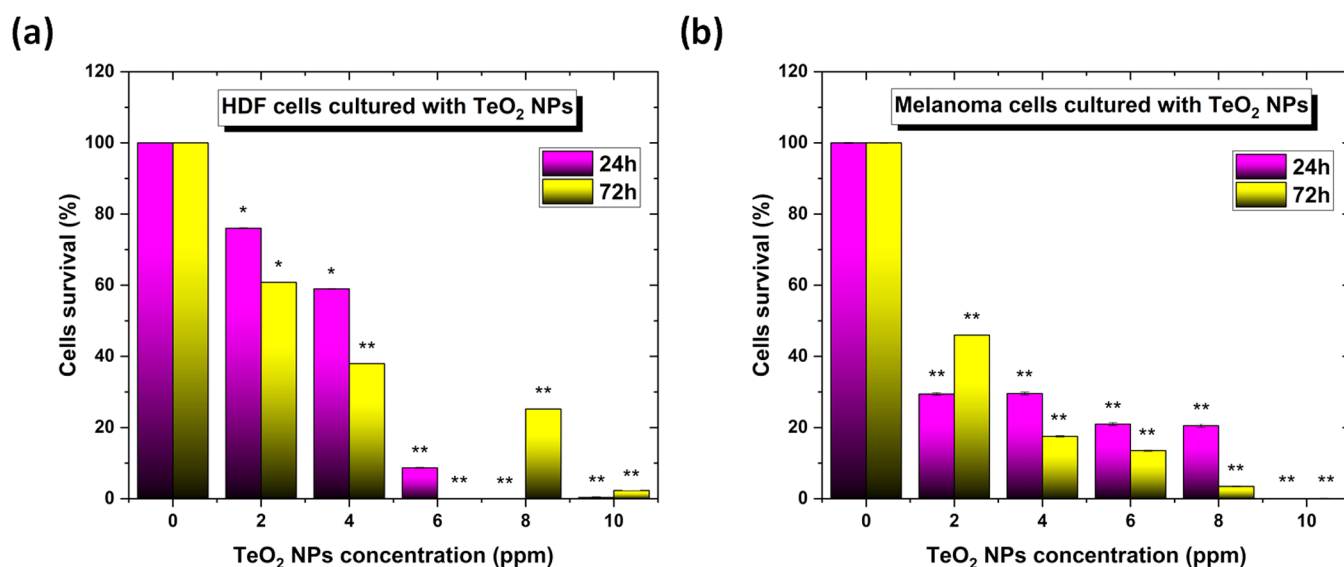
**Figure 8.** (a) Human dermal fibroblast (HDF) cells and (b) human melanoma cells in the presence of different concentrations of the NPs. $N = 3$. Data are represented as mean $\pm$ SD; *$p < 0.05$, **$p < 0.01$ compared to the control.
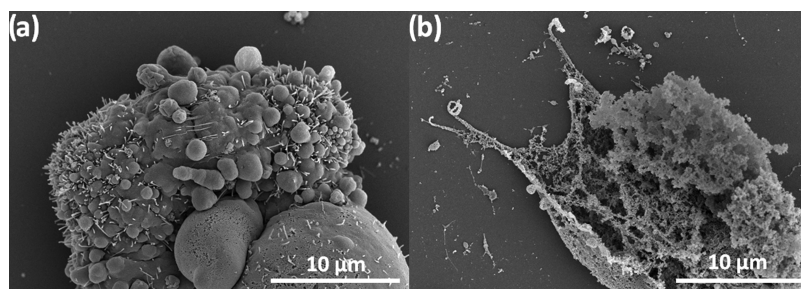


**Figure 9.** (a) Representative electron microscopy image of human melanoma cells before their interaction with the $TeO_2$ NPs. (b) Representative electron microscopy image of human melanoma cells after being exposed to a fixed concentration of 4 ppm of $TeO_2$ NPs; image is taken after 24 h of contact.

0.2 ppm for MDR *E. coli* and MR *S. aureus*, respectively. These values are in correlation with similar nanostructures of Te, such as Te/Te oxide NPs,[42] Te nanorods,[56] and composites of gold and silver with Te.[57]

To then assess the cytocompatibility of the NPs, cell studies were performed with HDF and human melanoma cells as in vitro models for potential skin treatments (Figure 8). The half-maximal inhibitory concentration (IC50) values were calculated with the aim to study the potency of the $TeO_2$ NPs to inhibit the growth of both HDF and human melanoma cells. These values were found at 5.5 $\pm$ 0.2 and 1.6 $\pm$ 0.7 ppm for HDF and human melanoma cells, respectively. These IC50 values are in concordance with similar nanostructures based on Te found in the literature and show that the NPs can be safely used in the presence of HDF cells and cause a remarkable cytotoxic behavior when exposed to human melanoma cells.[21,42,58]

SEM microscopy of human melanoma cells exposed to a concentration of 4 ppm of NPs showed signs of necrosis and apoptosis all over the cells. Visual cues, such as smoothing, loss of microvillous structures, blebbing, and shrinking, are often markers of apoptosis (Figure 9a),[59] while necrosis can be observed in those cells that partially disintegrate, leaving granular particles (Figure 9b).[60]

Lastly, to elucidate the potential mechanism of action, a reactive oxygen species (ROS) test was conducted in the presence of human melanoma cells. The four ROS types are the superoxide radical ($O_2^-$), the hydroxyl radical ($^\bullet OH$), hydrogen peroxide ($H_2O_2$), and singlet oxygen ($O_2$).[55] Results indicated that there is a significant release of ROS from the NPs to the cell media even at the lowest concentrations compared with the controls and that it linearly increases with larger amounts of NPs present in the media (Figure 10). These findings are in concordance with previously published studies by Gupta et al.,[61] who showed that the antimicrobial effects of $TeO_2$ NPs were attributed to the generation of ROS inside the bacterial cells.

**3.3. Mechanism of Tellurium Dioxide Formation.** The solvent in PLAL (DI water in our case) confines the plasma plume and also provides a reactive medium to generate a compound based on the target's chemical element,[62] in this case, Te. When the laser beam hits the Te target, it starts releasing Te into the solvent and it also breaks down water molecules located on the beam path according to the water splitting reaction[63]

$$2H_2O \rightarrow 2H_2 + O_2 \qquad (1)$$

When the plasma cools down (the laser beam is off), Te, $H_2$, and $O_2$ start reacting together to form Te-based compounds according to the following chemical reactions
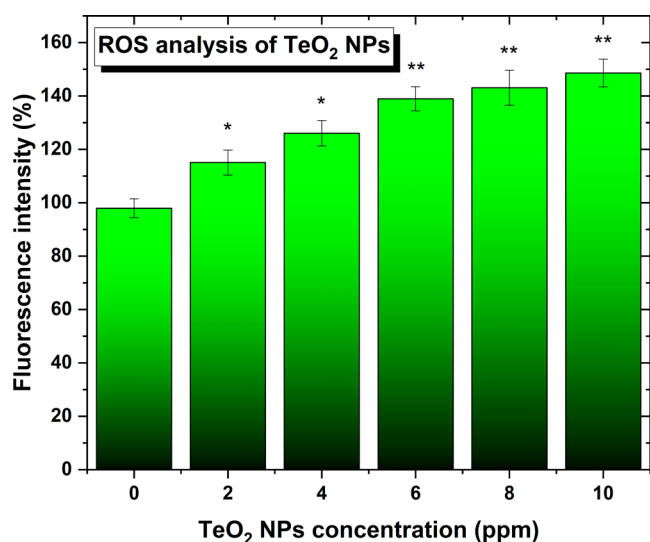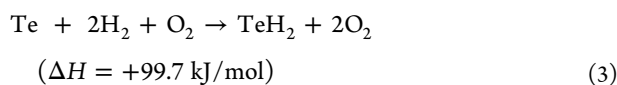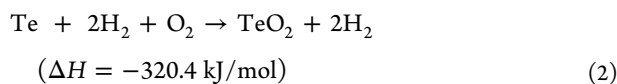
**Figure 10.** Reactive oxygen species (ROS) induced by the NPs in human melanoma cell experiments. A trend of the release of the species with the increase in NP concentration for the same time frame is seen. $N = 3$. Data is represented as mean $\pm$ SD; $*p < 0.05$, $**p < 0.01$ (compared to 0 concentration).

$$Te + 2H_2 + O_2 \rightarrow TeO_2 + 2H_2$$
$$(\Delta H = -320.4 \text{ kJ/mol}) \qquad (2)$$

$$Te + 2H_2 + O_2 \rightarrow TeH_2 + 2O_2$$
$$(\Delta H = +99.7 \text{ kJ/mol}) \qquad (3)$$

Based on the species present during the irradiation, Te will react preferentially with $O_2$ because the enthalpy of formation of $TeO_2$ is more negative than that of tellurium hydride ($TeH_2$), meaning that $TeO_2$ is expected to form, as observed experimentally in Section 3.1. Furthermore, the diatomic bond enthalpy of Te–O ($\sim$376.1 $\pm$ 20.9 kJ/mol) is larger than that of Te–Te ($\sim$259.8 $\pm$ 5.0 kJ/mol), meaning that Te prefers to bind with oxygen than Te.[64]

The oxidation of tellurium during the PLAL synthesis is caused by reactive oxygen species due to the decomposition of water molecules during irradiation. Indeed, the breakdown of the water molecules occurs because of the high-temperature plasma plume generated by the laser–target interactions. This phenomenon has already been observed in the formation of nanoparticles by PLAL.[63,65,66]

## 4. CONCLUSIONS

Here, an infrared nanosecond pulsed laser emitting at 1064 nm was used to irradiate a pure Te target immersed in DI water. The irradiation lasted only 5 min at 1 kHz, and spherical $\alpha$-$TeO_2$ NPs were successfully synthesized by PLAL. The presence of Te chunks/dust in the colloid comes directly from the target by being mechanically ejected when the laser beam hits the Te target. Due to the presence of two chalcogenide elements, O and Te, $TeO_2$ NPs were found to be toxic for microorganisms such as MDR *E. coli* and MR *S. aureus* at very low concentrations of $\sim$10 ppm. This can be understood by the similarity of the Te chemistry to S, as they both belong to the chalcogen family (O, S, Se, and Te). Indeed, Te can be incorporated into S-containing amino acids (such as cysteine and methionine), which are semi-essential

and essential amino acids for bacterial function, respectively. Then, those amino acids, which comprise proteins and enzymes, can consequently disrupt the metabolism of the bacteria. Moreover, $TeO_2$ NPs displayed a greater cytotoxic effect against human melanoma cells than human dermal fibroblasts. More work is currently underway to design other Te-based nanodrugs by PLAL and to further elucidate the mechanism by which these novel $TeO_2$ NPs kill antibiotic-resistant bacteria and cancer cells.

## ■ AUTHOR INFORMATION

### Corresponding Author
**Grégory Guisbiers** − *Department of Physics and Astronomy, University of Arkansas at Little Rock, Little Rock, Arkansas 72204, United States;* ● orcid.org/0000-0002-4615-6014; Email: gxguisbiers@ualr.edu

### Authors
**Tina Hesabizadeh** − *Department of Physics and Astronomy, University of Arkansas at Little Rock, Little Rock, Arkansas 72204, United States*

**Evan Hicks** − *Department of Physics and Astronomy, University of Arkansas at Little Rock, Little Rock, Arkansas 72204, United States*

**David Medina Cruz** − *Department of Chemical Engineering, Northeastern University, Boston, Massachusetts 02115, United States;* ● orcid.org/0000-0002-7658-583X

**Shawn E. Bourdo** − *Center for Integrative Nanotechnology Sciences, University of Arkansas at Little Rock, Little Rock, Arkansas 72204, United States;* ● orcid.org/0000-0002-9302-2094

**Fumiya Watanabe** − *Center for Integrative Nanotechnology Sciences, University of Arkansas at Little Rock, Little Rock, Arkansas 72204, United States*

**Marvin Bonney** − *Department of Physics and Astronomy, University of Arkansas at Little Rock, Little Rock, Arkansas 72204, United States*

**John Nichols** − *Department of Physics and Astronomy, University of Arkansas at Little Rock, Little Rock, Arkansas 72204, United States*

**Thomas J. Webster** − *Department of Chemical Engineering, Northeastern University, Boston, Massachusetts 02115, United States*

Complete contact information is available at:
https://pubs.acs.org/10.1021/acsomega.2c02316

### Author Contributions

T.H. (txhesabizade@ualr.edu): investigation (synthesis, UV–visible spectroscopy, Raman spectroscopy, DLS, $\zeta$-potential, SEM, and EDX) and formal analysis; E.H. (edhicks@ualr.edu): investigation (synthesis, DLS, and $\zeta$-potential); D.M.-C. (davidmedinacrz@gmail.com): investigation (antibacterial and anticancer properties, SEM) and formal analysis; S.E.B. (sxbourdo@ualr.edu): investigation (DSC), formal analysis, and validation; F.W. (fxwatanabe@ualr.edu): investigation (XPS), formal analysis, and validation; M.B. (mmbonney@ualr.edu): investigation (XRD) and formal analysis; J.N. (jxnichols@ualr.edu): investigation (XRD), formal analysis, and validation; T.J.W. (websterthomas02@gmail.com): validation and writing—reviewing and editing; and G.G. (gxguisbiers@ualr.edu): conceptualization, resources, visualization, validation, writing—reviewing and editing, formal analysis, funding acquisition, and project administration.

## Notes

The authors declare the following competing financial interest(s): The authors declare that the University of Arkansas at Little Rock has filled a provisional US patent on those tellurium dioxide nanoparticles.

## REFERENCES

(1) Ibers, J. Tellurium in a twist. *Nat. Chem.* **2009**, *1*, No. 508.

(2) Goldfarb, R. J. *Tellurium: Providing a Bright Future for Solar Energy*, U. S. Geological Survey, Fact Sheet 2014-3077, 2015.

(3) Chivers, T.; Laitinen, R. S. Tellurium: a maverick among the chalcogens. *Chem. Soc. Rev.* **2015**, *44*, 1725−1739.

(4) Geoffrion, L. D.; Guisbiers, G. Physico-chemical properties of selenium−tellurium alloys across the scales. *Nanoscale Adv.* **2021**, *3*, 4254−4270.

(5) Anderson, D. L. *Theory of the Earth*; Blackwell Scientific Publications, 1989.

(6) Mahabaduge, H. P.; Rance, W. L.; Burst, J. M.; Reese, M. O.; Meysing, D. M.; Wolden, C. A.; Li, J.; Beach, J. D.; Gessert, T. A.; Metzger, W. K.; et al. High-efficiency, flexible CdTe solar cells on ultra-thin glass substrates. *Appl. Phys. Lett.* **2015**, *106*, No. 133501.

(7) He, Y.; Zhang, T.; Shi, X.; Wei, S.-H.; Chen, L. High thermoelectric performance in copper telluride. *NPG Asia Mater.* **2015**, *7*, No. e210.

(8) Snyder, G. J.; Snyder, A. H. Figure of merit ZT of a thermoelectric device defined from materials properties. *Energy Environ. Sci.* **2017**, *10*, 2280−2283.

(9) Cunha, R. L. O. R.; Gouvea, I. E.; Juliano, L. A glimpse on biological activities of tellurium compounds. *An. Acad. Bras. Cienc.* **2009**, *81*, 393−407.

(10) Ba, L. A.; Döring, M.; Jamier, V.; Jacob, C. Tellurium: an element with great biological potency and potential. *Org. Biomol. Chem.* **2010**, *8*, 4203−4216.

(11) Knockaert, G. Tellurium and Tellurium Compounds. *Ullmann's Encycl. Ind. Chem.* **2011**, *35*, 685−695.

(12) Deringer, V. L.; Stoffel, R. P.; Dronskowski, R. Thermochemical Ranking and Dynamic Stability of TeO2 Polymorphs from Ab Initio Theory. *Cryst. Growth Des.* **2014**, *14*, 871−878.

(13) Ceriotti, M.; Pietrucci, F.; Bernasconi, M. Ab initio study of the vibrational properties of crystalline TeO$_2$: The $\alpha$, $\beta$, and $\gamma$ phases. *Phys. Rev. B* **2006**, *73*, No. 104304.

(14) Li, Y.; Fan, W.; Sun, H.; Cheng, X.; Li, P.; Zhao, X. Structural, electronic, and optical properties of $\alpha$, $\beta$, and $\gamma$−TeO2. *J. Appl. Phys.* **2010**, *107*, No. 093506.

(15) Moufok, S.; Kadi, L.; Amrani, B.; Khodja, K. D. Electronic structure and optical properties of TeO2 polymorphs. *Results Phys.* **2019**, *13*, No. 102315.

(16) Jha, A.; Richards, B. D. O.; Jose, G.; Fernandez, T. T.; Hill, C. J.; Lousteau, J.; Joshi, P. Review on structural, thermal, optical and spectroscopic properties of tellurium oxide based glasses for fibre optic and waveguide applications. *Int. Mater. Rev.* **2012**, *57*, 357−382.

(17) Fleming, A. On the specific antibacterial properties of penicillin and potassium tellurite. Incorporating a method of demonstrating some bacterial antagonisms. *J. Pathol. Bacteriol.* **1932**, *35*, 831−842.

(18) Lin, Z.-H.; Lee, C.-H.; Chang, H.-Y.; Chang, H.-T. Antibacterial Activities of Tellurium Nanomaterials. *Chem. - Asian J.* **2012**, *7*, 930−934.

(19) Miola, M.; Massera, J.; Cochis, A.; Kumar, A.; Rimondini, L.; Vernè, E. Tellurium: A new active element for innovative multifunctional bioactive glasses. *Mater. Sci. Eng., C* **2021**, *123*, No. 111957.

(20) Vahidi, H.; Kobarfard, F.; Alizadeh, A.; Saravanan, M.; Barabadi, H. Green nanotechnology-based tellurium nanoparticles: Exploration of their antioxidant, antibacterial, antifungal and cytotoxic potentials against cancerous and normal cells compared to potassium tellurite. *Inorg. Chem. Commun.* **2021**, *124*, No. 108385.

(21) Medina-Cruz, D.; Tien-Street, W.; Zhang, B.; Huang, X.; Vernet-Crua, A.; Nieto-Arguello, A.; Cholula-Diaz, J. L.; Martinez, L.; Huttel, Y.; Ujue Gonzalez, M.; et al. Citric juice-mediated synthesis of tellurium nanoparticles with antimicrobial and anticancer properties. *Green Chem.* **2019**, *21*, 1982−1998.

(22) Brown, C. D.; Cruz, D. M.; Roy, A. K.; Webster, T. J. Synthesis and characterization of PVP-coated tellurium nanorods and their antibacterial and anticancer properties. *J. Nanopart. Res.* **2018**, *20*, No. 254.

(23) Vernet-Crua, A.; Medina, D.; Zhang, B.; Gonzalez, M. U.; Huttel, Y.; Garcia-Martin, J. M.; Diaz, J. L. C.; Webster, T. J. Comparison of cytocompatibility and anticancer properties of traditional and green chemistry-synthesized tellurium nanowires. *Int. J. Nanomed.* **2019**, *14*, 3155−3176.

(24) El-Sayyad, G. S.; Mosallam, F. M.; El-Sayed, S. S.; El-Batal, A. I. Facile Biosynthesis of Tellurium Dioxide Nanoparticles by Streptomyces cyaneus Melanin Pigment and Gamma Radiation for Repressing Some Aspergillus Pathogens and Bacterial Wound Cultures. *J. Cluster Sci.* **2020**, *31*, 147−159.

(25) Zhang, H.; Swihart, M. T. Synthesis of Tellurium Dioxide Nanoparticles by Spray Pyrolysis. *Chem. Mater.* **2007**, *19*, 1290−1301.

(26) Jung, T.-K.; Ryou, M.; Lee, J.-W.; Hyun, S.-K.; Na, H. G.; Jin, C. Comparison of Structural and Optical Properties of TeO2 Nanostructures Synthesized Using Various Substrate Conditions. *Met. Mater. Int.* **2017**, *23*, 1133−1138.

(27) Arab, F.; Mousavi-Kamazani, M.; Salavati-Niasari, M. Facile sonochemical synthesis of tellurium and tellurium dioxide nanoparticles: Reducing Te(IV) to Te via ultrasonic irradiation in methanol. *Ultrason. Sonochem.* **2017**, *37*, 335−343.

(28) Liu, J.; Liang, C.; Zhu, X.; Lin, Y.; Zhang, H.; Wu, S. Understanding the Solvent Molecules Induced Spontaneous Growth of Uncapped Tellurium Nanoparticles. *Sci. Rep.* **2016**, *6*, No. 32631.

(29) Guisbiers, G.; Mimun, L. C.; Mendoza-Cruz, R.; Nash, K. L. Synthesis of tunable tellurium nanoparticles. *Semicond. Sci. Technol.* **2017**, *32*, No. 04LT01.

(30) Forsythe, R. C.; Cox, C. P.; Wilsey, M. K.; Müller, A. M. Pulsed Laser in Liquids Made Nanomaterials for Catalysis. *Chem. Rev.* **2021**, *121*, 7568−7637.

(31) Taylor, P.; Kusper, M.; Hesabizadeh, T.; Geoffrion, L. D.; Watanabe, F.; Herth, E.; Guisbiers, G. Synthesis of naked vanadium pentoxide nanoparticles. *Nanoscale Adv.* **2021**, *3*, 1954−1961.

(32) Batista, L. M. F.; Kunzler, K.; John, M. G.; Clark, B.; Bullock, A.; Ferri, J.; Gupton, B. F.; Tibbetts, K. M. Laser synthesis of uncapped palladium nanocatalysts. *Appl. Surf. Sci.* **2021**, *557*, No. 149811.

(33) Geoffrion, L. D.; Hesabizadeh, T.; Medina-Cruz, D.; Kusper, M.; Taylor, P.; Vernet-Crua, A.; Chen, J.; Ajo, A.; Webster, T. J.; Guisbiers, G. Naked selenium nanoparticles for antibacterial and anticancer treatments. *ACS Omega* **2020**, *5*, 2660−2669.

(34) Geoffrion, L. D.; Medina-Cruz, D.; Kusper, M.; Elsaidi, S.; Watanabe, F.; Parajuli, P.; Ponce, A.; Hoang, T. B.; Brintlinger, T. H.; Webster, T. J.; Guisbiers, G. Bi2O3 nano-flakes as a cost-effective antibacterial agent. *Nanoscale Adv.* **2021**, *3*, 4106−4118.

(35) Guisbiers, G.; Wang, Q.; Khachatryan, E.; Arellano-Jimenez, M. J.; Webster, T. J.; Larese-Casanova, P.; Nash, K. L. Anti-bacterial selenium nanoparticles produced by UV/VIS/NIR pulsed nanosecond laser ablation in liquids. *Laser Phys. Lett.* **2014**, *12*, No. 016003.

(36) Nikolov, A. S.; Balchev, I. I.; Nedyalkov, N. N.; Kostadinov, I. K.; Karashanova, D. B.; Atanasova, G. B. Influence of the laser pulse repetition rate and scanning speed on the morphology of Ag nanostructures fabricated by pulsed laser ablation of solid target in water. *Appl. Phys. A* **2017**, *123*, No. 719.

(37) Khalef, W. K. Preparation and Characterization of Teo2 Nano particles by Pulsed Laser Ablation in Water. *Eng. Technol. J.* **2014**, *32*, 396−405.

(38) Private communication between Guisbiers and Liang - Email: Questions about your Scientific Reports paper published in 2016. 2021.

(39) Saraeva, I. N.; Tolordava, E. R.; Nastulyavichus, A. A.; Ivanova, A. K.; Kudryashov, S. I.; Rudenko, A. A.; Melnik, N. N.; Zayarny, D. A.; Ionin, A. A.; Romanova, Y. M.; Gonchukov, S. A. A bacterial misericorde: laser-generated silicon nanorazors with embedded biotoxic nanoparticles combat the formation of durable biofilms. *Laser Phys. Lett.* **2020**, *17*, No. 025601.

(40) Khalef, W. K.; Marzoog, T. R.; Faisal, A. D. Synthesis and characterization of tellurium oxide nanoparticles using pulse laser ablation and study their antibacterial activity. *J. Phys.: Conf. Ser.* **2021**, *1795*, No. 012049.

(41) Hamad, A.; Li, L.; Liu, Z. Comparison of characteristics of selected metallic and metal oxide nanoparticles produced by picosecond laser ablation at 532 and 1064 nm wavelengths. *Appl. Phys. A* **2016**, *122*, No. 904.

(42) Medina-Cruz, D.; Vernet-Crua, A.; Mostafavi, E.; González, M. U.; Martínez, L.; Jones, A.-A. D., III; Kusper, M.; Sotelo, E.; Gao, M.; Geoffrion, L. D.; et al. Aloe Vera-Mediated Te Nanostructures: Highly Potent Antibacterial Agents and Moderated Anticancer Effects. *Nanomaterials* **2021**, *11*, No. 514.

(43) https://www.abcam.com/cellular-ros-assay-kit-red-ab186027. html.

(44) Smith, W.; Tyndall, A. J. *Sci. Mon.* **1920**, *11*, 331−340.

(45) Kraemer, E. O.; Dexter, S. T. The Light-Scattering Capacity (Tyndall Effect) and Colloidal Behavior of Gelatine Sols and Gels. *J. Phys. Chem. A* **1927**, *31*, 764−782.

(46) Rodriguez, V.; Couzi, M.; Adamietz, F.; Dussauze, M.; Guery, G.; Cardinal, T.; Veber, P.; Richardson, K.; Thomas, P. Hyper-Raman and Raman scattering in paratellurite TeO₂. *J. Raman Spectrosc.* **2013**, *44*, 739−745.

(47) Jafari, A.; Klobes, B.; Sergueev, I.; Moseley, D. H.; Manley, M. E.; Dronskowski, R.; Deringer, V. L.; Stoffel, R. P.; Bessas, D.; Chumakov, A. I.; et al. Phonon Spectroscopy in Antimony and Tellurium Oxides. *J. Mater. Chem. A* **2020**, *124*, 7869−7880.

(48) Gupta, N.; Kaur, A.; Khanna, A.; Gonzàlez, F.; Pesquera, C.; Iordanova, R.; Chen, B. Structure-property correlations in TiO2-Bi2O3-B2O3-TeO2 glasses. *J. Non-Cryst. Solids* **2017**, *470*, 168−177.

(49) Charton, P.; Gengembre, L.; Armand, P. TeO₂-WO₃ Glasses: Infrared, XPS and XANES Structural Characterizations. *J. Solid State Chem.* **2002**, *168*, 175−183.

(50) https://www.thermofisher.com/us/en/home/materials-science/learning-center/periodic-table/metalloid/tellurium.html.

(51) Guisbiers, G. Advances in thermodynamic modelling of nanoparticles. *Adv. Phys.: X* **2019**, *4*, No. 1668299.

(52) Guisbiers, G. Size-dependent materials properties toward a universal equation. *Nanoscale Res. Lett.* **2010**, *5*, 1132−1136.

(53) Dolai, J.; Mandal, K.; Jana, N. R. Nanoparticle Size Effects in Biomedical Applications. *ACS Appl. Nano Mater.* **2021**, *4*, 6471−6496.

(54) Zannoni, D.; Borsetti, F.; Harrison, J. J.; Turner, R. J. The Bacterial Response to the Chalcogen Metalloids Se and Te. In *Advances in Microbial Physiology*; Elsevier, 2007; Vol. *53*, pp 1−312.

(55) Wang, L.; Hu, C.; Shao, L. The antimicrobial activity of nanoparticles: present situation and prospects for the future. *Int. J. Nanomed.* **2017**, *12*, 1227−1249.

(56) Shakibaie, M.; Adeli-Sardou, M.; Mohammadi-Khorsand, T.; Zeydabadi-Nejad, M.; Amirafzali, E.; Amirpour-Rostami, S.; Ameri, A.; Forootanfar, H. Antimicrobial and Antioxidant Activity of the

Biologically Synthesized Tellurium Nanorods; A Preliminary In vitro Study. *Iran. J. Biotechnol.* **2017**, *15*, 268−276.

(57) Chang, H.-Y.; Cang, J.; Roy, P.; Chang, H.-T.; Huang, Y.-C.; Huang, C.-C. Synthesis and antimicrobial activity of gold/silver-tellurium nanostructures. *ACS Appl. Mater. Interfaces* **2014**, *6*, 8305−8312.

(58) Huang, W.; He, L.; Ouyang, J.; Chen, Q.; Liu, C.; Tao, W.; Chen, T. Triangle-Shaped Tellurium Nanostars Potentiate Radiotherapy by Boosting Checkpoint Blockade Immunotherapy. *Matter* **2020**, *3*, 1725−1753.

(59) Pesce, M.; De Felici, M. Apoptosis in mouse primordial germ cells: a study by transmission and scanning electron microscope. *Anat. Embryol.* **1994**, *189*, 435−440.

(60) Cabral, G. A.; Toney, D. M.; Fischer-Stenger, K.; Harrison, M. P.; Marciano-Cabral, F. Anandamide inhibits macrophage-mediated killing of tumor necrosis factor-sensitive cells. *Life Sci.* **1995**, *56*, 2065−2072.

(61) Gupta, P. K.; Sharma, P. P.; Sharma, A.; Khan, Z. H.; Solanki, P. R. Electrochemical and antimicrobial activity of tellurium oxide nanoparticles. *Mater. Sci. Eng.: B* **2016**, *211*, 166−172.

(62) Yan, Z.; Chrisey, D. B. Pulsed laser ablation in liquid for micro-/nanostructure generation. *J. Photochem. Photobiol., C* **2012**, *13*, 204−223.

(63) Barmina, E. V.; Gudkov, S. V.; Simakin, A. V.; Shafeev, G. A. Stable Products of Laser-Induced Breakdown of Aqueous Colloidal Solutions of Nanoparticles. *J. Laser Micro/Nanoeng.* **2017**, *12*, 254−257.

(64) https://www.webelements.com/tellurium/compound_properties.html.

(65) Marzun, G.; Bönnemann, H.; Lehmann, C.; Spliethoff, B.; Weidenthaler, C.; Barcikowski, S. Role of Dissolved and Molecular Oxygen on Cu and PtCu Alloy Particle Structure during Laser Ablation Synthesis in Liquids. *ChemPhysChem* **2017**, *18*, 1175−1184.

(66) Kalus, M.-R.; Lanyumba, R.; Lorenzo-Parodi, N.; Jochmann, M. A.; Kerpen, K.; Hagemann, U.; Schmidt, T. C.; Barcikowski, S.; Gökce, B. Determining the role of redox-active materials during laser-induced water decomposition. *Phys. Chem. Chem. Phys.* **2019**, *21*, 18636−18651.